



ORIGINAL ARTICLE

Synthesis and properties of alginate-based nanoparticles incorporated with different inorganic nanoparticulate modifiers for enhanced encapsulation and controlled release of favipiravir



Sreekanth Reddy Obireddy^{a,b,*}, Shirisha Bellala^b, Madhavi Chintha^c,
Akkulanna Sake^d, Subha Marata Chinna Subbarao^b, Wing-Fu Lai^{a,e,*}

^a Department of Applied Biology and Chemical Technology, Hong Kong Polytechnic University, Hong Kong Special Administrative Region, China

^b Department of Chemistry, Sri Krishnadevaraya University, Ananthapuramu 515003, India

^c Department of Polymer Science and Technology, Sri Krishnadevaraya University, Ananthapuramu 515003, India

^d Department of Botany, Sri Krishnadevaraya University, Ananthapuramu 515003, India

^e Department of Urology, Zhejiang Provincial People's Hospital, Hangzhou Medical College, Zhejiang 310012, China

Received 1 June 2022; accepted 24 February 2023

Available online 2 March 2023

KEYWORDS

Alginate;
Sustained release;
Silver nanoparticles;
Magnetic nanoparticles;
Montmorillonite;
Drug encapsulation

Abstract Alginate is a naturally occurring polysaccharide that consists of guluronic and manuronic acid residues. Although it has been widely exploited in drug delivery because of its favorable properties (biocompatibility, ease of processing, and gelling capability under mild conditions), most alginate-based systems show poor sustained-release drug release because of the high erosion rate of alginate-based hydrogels. This study exploited the effect of three inorganic nanoparticulate modifiers (including montmorillonite clay material, silver nanoparticles, and iron-based magnetic nanoparticles) on the encapsulation and controlled release of favipiravir, which served as a model for poorly soluble drugs. Structures of the generated nanoparticles were characterized by using UV-visible spectroscopy, X-ray diffraction (XRD), Fourier transform infrared spectroscopy (FTIR), scanning electron microscope (SEM), and thermogravimetric analysis (TGA) to examine interactions between the loaded drug and the components of the nanoparticles. The incorporation of various nanoparticulate modifiers into alginate-based nanoparticles had little effect on the drug release mechanism, with all modified nanoparticles following a Super Case-II transport mechanism in

* Corresponding author.

E-mail addresses: rori0610@graduate.hku.hk (W.F. Lai), sreekanthchem7@gmail.com (S. Reddy Obireddy).

Peer review under responsibility of King Saud University.



which the drug release rate was governed by the relaxation of the polymeric chains. However, nanoparticles incorporated with different modifiers show variations in porosity and hydrophilicity. This caused ultimate changes in drug encapsulation efficiency and release sustainability.

© 2023 The Author(s). Published by Elsevier B.V. on behalf of King Saud University. This is an open access article under the CC BY-NC-ND license (<http://creativecommons.org/licenses/by-nc-nd/4.0/>).

1. Introduction

Targeted drug delivery using polymeric matrices has been showing a remarkable growth with due to their extensive availability in nature, biodegradability, non-toxicity, and good biocompatibility (Elmowafy et al., 2019, Sung and Kim 2020). Polymer-based hydrogels are essential in a wide range of biomedical applications. Sodium alginate (SA), one of the polymers, is derived from brown algae composed of random sequences of β -D-mannuronic acid (M block) and α -L-guluronic acid (G-block) residues (Jiao et al., 2019). It has great biocompatibility, easy processing, and gelling capability under mild conditions, and hence is extensively used in food and pharmaceutical applications (Abasalizadeh et al., 2020). Moreover, alginate is an excellent matrix for the prolonged release of a variety of pharmacological compounds. SA matrices are extensively used in the manufacturing of controlled and sustained release formulations because they are rapidly destroyed and absorbed by the body during and after drug molecule release (Lee and Mooney 2012, Reddy et al., 2019).

Despite the potential use of alginate in drug delivery, most of the alginate-based systems show poor drug release sustainability because of the high erosion rate of alginate-based hydrogels. To enhance the performance of alginate-based carriers, a number of modifiers, such as clay materials, have been adopted over the years. Clay materials have been used for a long time in pharmaceutical formulations as disintegrants, diluting agents, pigments, and binders for many different materials (Carretero and Pozo 2009). They have long been used to treat a variety of ailments, including food poisoning, aches and pains, infections, and mineral deficiencies (Carretero and Pozo 2009). In recent years, researchers have become more interested in using montmorillonite (MMT) in pharmaceutical formulations because of its high adsorption capacity, large surface area, strong adhesive capacity, ability to intercalate large molecules into space, and ability to carry bioactive agents (Huang et al., 2017, Krupskaya et al., 2017, Li et al., 2018). Typically, simple ionotropic gelation procedures are employed to encapsulate hydrophilic medicines in polymeric hydrogel beads, but this method has low encapsulation efficacy for drugs that show minimal solubility in water. In this study, MMT clay material is studied as one of the inorganic nanoparticulate modifiers to improve the encapsulation and sustained release of favipiravir (FPV), which serves as a model of poorly soluble drugs. Since MMT clay material is mucoadhesive, drug molecules can be inserted into it, leading to improved drug encapsulation efficiency (Hun Kim et al., 2016).

Apart from using MMT clay material, this study exploits the use of silver-based nanoparticles (NPs) as modifiers for alginate-based nanoparticles for FPV delivery. Nanoparticles have been synthesized using a wide variety of synthetic processes, the most popular of which are physical, chemical, and biosynthetic. Conventional chemical approaches are sometimes prohibitively expensive and involve the use of harmful and poisonous substances that are directly or indirectly responsible for a number of environmental hazards (Chandrakala et al., 2022, Samuel et al., 2022). The biosynthetic method provides a safe, biocompatible, environmentally friendly, and green method for synthesizing nanoparticles for biomedical applications using plants and microorganisms. This green synthesis is possible with fungi, algae, bacteria, and plants. The phytochemicals present in the extract of some plant parts, such as leaves, fruits, roots, stems, and seeds, have been employed in the production of different nanoparticles. These phytochemicals work as stabilizing and reducing agents. Silver is an elemen-

tal metal that exhibits a broad spectrum of antibacterial activity against a variety of bacteria, fungi, and viruses. Many studies have shown that silver nanoparticles (AgNPs) can be used to fight viruses that are harmful to humans, like respiratory syncytial virus (RSV), influenza virus, norovirus, hepatitis B virus (HBV), and human immunodeficiency virus (HIV) (Galdiero et al., 2011). Additionally, silver has been shown to have a strong inhibitory effect on viral infection (Jeremiah et al., 2020). AgNPs have been shown to attach only to viral surface proteins that have sulfhydryl groups and break a disulfide bond, which weakens the protein and reduces viral infection (Jeremiah et al., 2020). The use of silver nanoparticles as carriers in drug delivery and their effect on the performance of alginate-based nanoparticles for encapsulation and controlled release of FPV will also be studied.

Finally, iron-based magnetic nanoparticles (MNPs) have a lot of advantages and show great promise in the treatment and detection of viral infections (Teja and Koh 2009, Jat et al., 2021), even though iron has been employed more commonly in biomedicine in the form of maghemite (Fe_2O_3 , $\gamma\text{-Fe}_2\text{O}_3$) or magnetite (Fe_3O_4) (Akbarzadeh et al., 2012). A recent study has found that iron oxide MNPs can help treat and prevent H1N1 virus infections (Kumar et al., 2019). Iron-based MNPs therefore serve as the third class of inorganic nanoparticulate modifiers for alginate-based nanoparticles in encapsulation and sustained release of FPV. In this study, we generated AgNPs, amine-MNPs (AMNPs), and MMT-based drug carriers to evaluate the effect of inorganic nanoparticulate modifiers on encapsulation, and *in vitro* release of FPV. The generated carriers are characterized by different techniques ranging from structural characterization to performance evaluation.

2. Experimental

2.1. Materials

MMT, ferric chloride hexahydrate, ferrous chloride tetrahydrate, ammonium hydroxide, and ethylenediamine were purchased from Sigma Aldrich, St. Louis, MO, USA. Sodium alginate, calcium chloride, and silver nitrate were purchased from Sd.Fine Chemicals, Mumbai, India. Favipiravir was received as a sample gift from Aspiro Pharma (Telangana, India). Double distilled water prepared in the laboratory was used throughout the experiment. The AMNPs were produced in accordance with our earlier research (Obireddy and Lai 2022). MMT was purified as per our previous research work (Obireddy et al., 2021).

2.2. Collection of the plant material (*Phyllanthus virgatus*)

The plant material was collected from the fields of Kalasamudram, Anantapuramu district, Andhra Pradesh, India. The leaves were washed with tap water and then distilled water to remove dust and other contaminants. They were then allowed to dry at room temperature for a day. Collected specimen was identified and deposited at Sri Krishnadevaraya University (SKU) Herbarium with voucher specimen No.50208.

2.3. Preparation of leaf extract

10 g of dried leaves were weighed and 100 mL of double distilled water was added and boiled for 30 min at 60 °C (Pirtarighat et al., 2019). After cooling the extract was filtered using Whatman No.1 filter paper and stored at 4 °C for further use (Fig. 1).

2.4. Preparation of 1 mM AgNO₃ solution

1 mM of silver nanoparticles were accurately prepared by dissolving 0.017 gms AgNO₃ in 100 mL of double distilled water and stored in an amber-coloured bottle to prevent auto oxidation of silver.

2.5. Green synthesis of silver NPs using *phyllanthus virgatus* leaf extract

2 mL of *P. virgatus* leaf extract was added to 200 mL of AgNO₃ (1 mM) solution and exposed to the sunlight for half an hour. The leaf extract acted as a reducing agent and the stabilized solution led to the formation of nanoparticles (Rizwana et al., 2022).

2.6. Synthesis of FPV-loaded SA-AgNPs, SA-AMNPs and SA-MMT microbeads

Briefly, 0.4 g of SA was transferred into 20 mL of distilled water and stirred overnight to get a clear solution. 0.2 g of AgNPs were added to this polymeric solution and then sonicated for 30 min. Afterwards, 0.2 g of FPV was added, sonicated for 5 min and stirred at 300 rpm for 6 h. The resulting solution was gradually transferred drop-wise into 5 % calcium chloride solution. Spherical microbeads were generated instantly and allowed for 30 min for crosslinking purpose. The obtained microbeads were washed several times with water to remove the drug adhered on the surface and allowed to dry at room temperature.

Similarly, FPV-loaded SA-AMNPs and MMT-intercalated polymeric microbeads were synthesized by the above procedure. During the preparation, instead of AgNPs, AMNPs and MMT were added separately, and the remaining process



Fig. 1 A photo showing the appearance of the plant extract, AgNO₃ solution, and AgNPs.

was the same as discussed above. SA microbeads were synthesized by the above-mentioned procedure without the addition of FPV and NPs.

2.7. Characterization techniques

The fabricated polymeric carriers were analyzed using Fourier transform infrared spectroscopy (FTIR) (model Bomem MB-3000, with Horizon MBTM FTIR software) within the wavelength region of 400–4000 cm⁻¹ to find out the interactions between the polymer matrix, FPV, MMT, AgNPs and AMNPs. UV–visible spectrum analysis was carried out to validate the generation of AgNPs. The thermal stability [thermogravimetric analysis (TGA) and differential scanning calorimetry (DSC)] of FPV, MMT, AgNPs, AMNPs, and drug-loaded microbeads was analyzed at a heating rate of 10 °C/min from 40 °C to 600 °C using a DTA analyzer (TA Instruments Q600 SDT) under an N₂ environment. X-ray diffraction (XRD) analysis (Model: Ultima IV X-Ray Diffractometer, Make: Rigaku, Japan) of FPV, AgNPs, AMNPs, MMT, and the developed drug carriers was performed at a scanning rate of 10°/min within the 2θ range of 5° to 80° with CuKα radiation (λ = 1.54060) to find out the crystalline nature and molecular dispersion of FPV molecules. Scanning electron microscope (SEM) (JOEL MODEL: JSM 840A) studies were conducted to determine the morphological structure of all fabricated microbeads.

2.8. Encapsulation efficiency (EE)

10 mg of FPV-loaded microbeads were transferred to 10 mL of phosphate-buffered saline (PBS). The suspension was agitated for 24 h at ambient temperature in a dark room. The microbeads were then crushed and sonicated for 10 min to extract all the FPV. Then the resultant suspension was centrifuged, the supernatant filtered, and the absorbance measured at 234 nm using a UV–Visible spectrometer (Boddu et al., 2022).

$$\%EE = \frac{\text{Amount of FPV in filtrate}}{\text{Amount of FPV added during preparation}} \times 100$$

2.9. In vitro FPV release

The *in vitro* drug release of all microbeads was determined by the following procedure. In brief, 100 mg of microbeads were put into a dialysis bag, and dropped into 500 mL of PBS at 37 °C at pH 2.0 and pH 6.8. At regular time intervals, the amount of FPV released was analysed using a UV–Visible spectrometer at 234 nm. Different release kinetic models, such as the zero order, first order, Higuchi, and Korsmeyer-Peppas models, were used to investigate the drug release kinetics and release mechanism of drug-loaded microbeads (Costa and Sousa Lobo 2001, Chintha et al., 2020).

3. Results and discussions

3.1. Structural analysis

An FTIR analysis was carried out in order to determine the interactions between the polymer, MMT, NPs, and FPV,

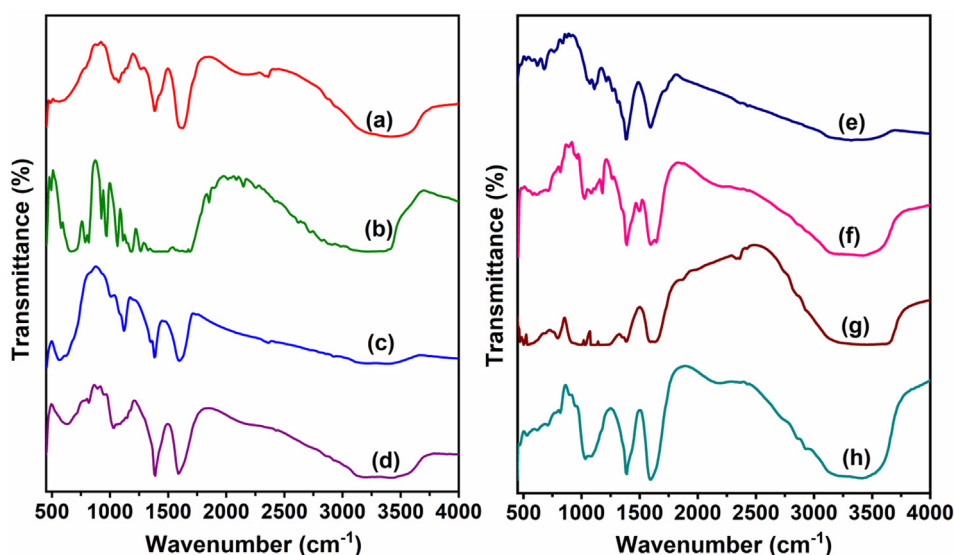


Fig. 2 FTIR spectra of a)SA, b)FPV, c)AMNPs, d) SA-AMNPs-FPV, e) AgNPs, f) SA-AgNPs-FPV, g) MMT and h) SA-MMT-FPV.

and the findings are shown in Fig. 2. The FTIR spectra of SA showed the following peaks at 3427 cm^{-1} (–O–H stretching frequency), 2857 cm^{-1} (stretching frequency of $\text{SP}^3\text{ C-H}$), 1598 cm^{-1} and 1387 cm^{-1} (asymmetric stretching frequencies of COO^- group), 1117 cm^{-1} and 1026 cm^{-1} (stretching frequencies of C–C group) (Li et al., 2008). The FTIR spectra of FPV showed the characteristic peaks at $3217\text{--}3355\text{ cm}^{-1}$ (stretching frequency of –N–H and –O–H), 2987 cm^{-1} (stretching frequency of aromatic C–H), 1655 , 1264 and 1183 cm^{-1} were due to C = O, C–F and C–O stretching frequency, respectively. The FTIR spectra of AMNPs showed the peaks at 573 cm^{-1} and 621 cm^{-1} (stretching frequency of Fe–O), 1597 cm^{-1} (stretching frequency of amine N–H) and 3394 cm^{-1} (stretching frequency of N–H). This suggested the successful incorporation of that amine groups onto the nanoparticle surface. These results suggested that amine functional groups were successfully present on the surface of MNPs (Obireddy and Lai 2022). By comparing the FTIR spectra of SA and SA-AMNPs, a distinct peak at 629 cm^{-1} was found, confirming the interaction between SA and AMNPs. Additionally, the SA peak at 1598 cm^{-1} was moved to 1587 cm^{-1} in SA-AMNPs, indicating that the FPV was loaded successfully into the microbeads. Furthermore, a new peak at 1037 cm^{-1} in SA-AMNPs microbeads demonstrated the existence of C–F stretching frequency, indicating that FPV was present in the polymer matrix. The FTIR spectra of AgNPs showed the peaks at 3413 cm^{-1} (stretching frequency of O–H or N–H), 3145 cm^{-1} (aromatic C–H stretching frequency), 1595 cm^{-1} (bending frequency of N–H), 1386 cm^{-1} (bending frequency of C–H), 1213 cm^{-1} (stretching frequency of C–O), and 1072 cm^{-1} (amine C–N stretching frequency). These amine, alcohol and aromatic groups were important for the stability and capping of AgNP, and similar observations were found in several studies (Niraimathi et al., 2013, Jyoti et al., 2016). By comparing the FTIR spectra of SA microbeads and SA-AgNPs-FPV, new peaks at 1642 , 1498 , and 1022 cm^{-1} were observed, which confirmed the taking place of an interaction between SA and AgNPs. Moreover, the peak at 1598 cm^{-1} in SA was shifted to 1596 cm^{-1} in SA-AgNPs-FPV, which indicated the successful loading of the FPV into

the microbeads. In addition, a new peak at 1071 cm^{-1} in SA-AgNPs-FPV microbeads indicated the presence of C–F stretching frequency, which confirmed the presence of FPV in the polymer matrix. The FTIR spectra of MMT showed the characteristic peaks at 3628 and 3524 cm^{-1} (stretching frequency of O–H of Si–OH and Al–Al–OH groups), 1628 cm^{-1} (bending frequency of H–O–H of adsorbed H_2O), 1386 , 1029 and 996 cm^{-1} (stretching frequency of Si–O–Si) and the peaks at 794 and 534 cm^{-1} corresponded to bending frequencies of O–Si–O and Al–Si–O groups (Zheng et al., 2017). In the FTIR spectra of MMT-loaded microbeads (SA-MMT-FPV), a peak at 3628 cm^{-1} of MMT clay had disappeared, which indicated that the polymer matrix interacted with the actives of MMT. In addition, the peak at 3524 cm^{-1} of MMT was shifted to a lower frequency in SA-MMT. This was another confirmation of the interaction of MMT with the polymer matrix. Furthermore, new peaks at 532 cm^{-1} , 624 cm^{-1} , and 709 cm^{-1} were observed in SA-MMT, which were characteristic peaks of MMT; this indicated that MMT had successfully interacted with the polymer matrix. In addition, a new peak at 1071 cm^{-1} was found in SA-MMT-FPV microbeads, which is due to C–F stretching frequency of PFV. This meant FPV was in the polymer matrix.

3.2. UV-visible spectroscopy analysis

The formation of AgNPs from AgNO_3 by green synthesis method using leaf extract of *P.virgatus* was confirmed by UV-visible spectroscopy. The appearance of a significant peak at $435\text{--}445\text{ nm}$ in the UV-visible spectroscopy spectrum indicated the conversion of silver ions into AgNPs (Fig. 3). These results were in good agreement with the results of Rautela et al. (Rautela et al., 2019), who made similar observations in their synthesis and characterization of silver nanoparticles.

3.3. DSC and TGA

The thermal analysis technique was used to find out the stability of the developed microbeads and the results were shown in Fig. 4. The thermal degradation of AgNPs curve showed the

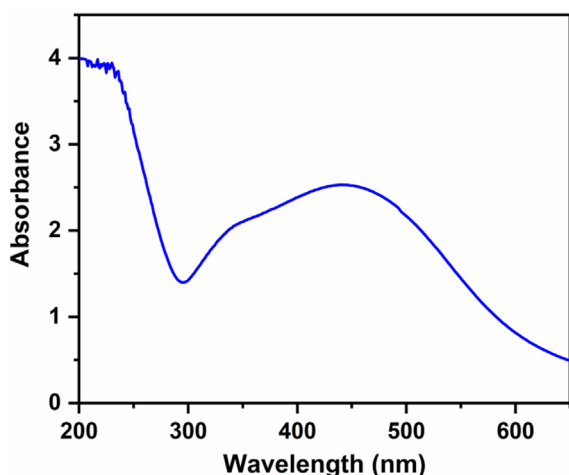


Fig. 3 UV-Vis absorption spectrum of AgNPs.

weight loss had occurred at 40–117 °C and 121–600 °C by 2% and 41%, respectively. The first loss was due to evaporation of adsorbed water molecules while the second loss was due to decomposition of capping organic compounds on AgNPs (Kota et al., 2017). The thermal degradation curve of MMT showed weight loss steps at 40–103 °C and 107–600 °C by 10% and 13 %, respectively. The first weight loss was due to evaporation of adsorbed water and the second loss was due to loss of structural water molecules (Zheng et al., 2017).

The TGA curve of AMNPs showed a weight loss of 6.5% at 40–600 °C due to dehydration of adsorbed water on AMNPs (Obireddy and Lai 2022). The thermal degradation curve of FPV showed that it was stable up to 168 °C after that its decomposition started. The thermal degradation curve of SA showed the weight loss at 40–188 °C, 191–306 °C, and 310–600 °C by 34%, 21%, and 9%, respectively. The first weight loss was due to dehydration of adsorbed water molecules, while the second and third were due to degradation of polymer matrix. After the incorporation of AMNPs, AgNPs and MMT into the polymer matrix, the weight loss of respective microbeads was $\sim 20\%$ less than that of SA, which indicated the presence of NPs and clay particles increased the stability of the microbeads (Thimmaiah et al., 2022).

The DSC technique was used to find the melting point and molecular dispersion of FPV and the phase transition of AMNPs and AgNPs and the thermograms were shown in Fig. 5. The DSC pattern of FPV showed two endothermic peaks at 193 and 238 °C, which indicated the melting point of FPV. The DSC of SA showed two endothermic peaks at 67 and 186 °C, which were due to dehydration of adsorbed moisture and melting temperature (T_m) of the SA microbeads. The DSC pattern of AMNPs showed an exothermic peak at 518 °C, which was due to the phase transition of $\gamma\text{-Fe}_2\text{O}_3$ to $\alpha\text{-Fe}_2\text{O}_3$, whereas this peak was not found in SA-AMNPs-FPV due to stabilization of AMNPs by the SA polymer matrix. The DSC pattern of AgNPs showed two peaks; an endothermic peak at 149 °C, which is due to the melting point of AgNPs, and another exothermic peak at 340 °C, while these

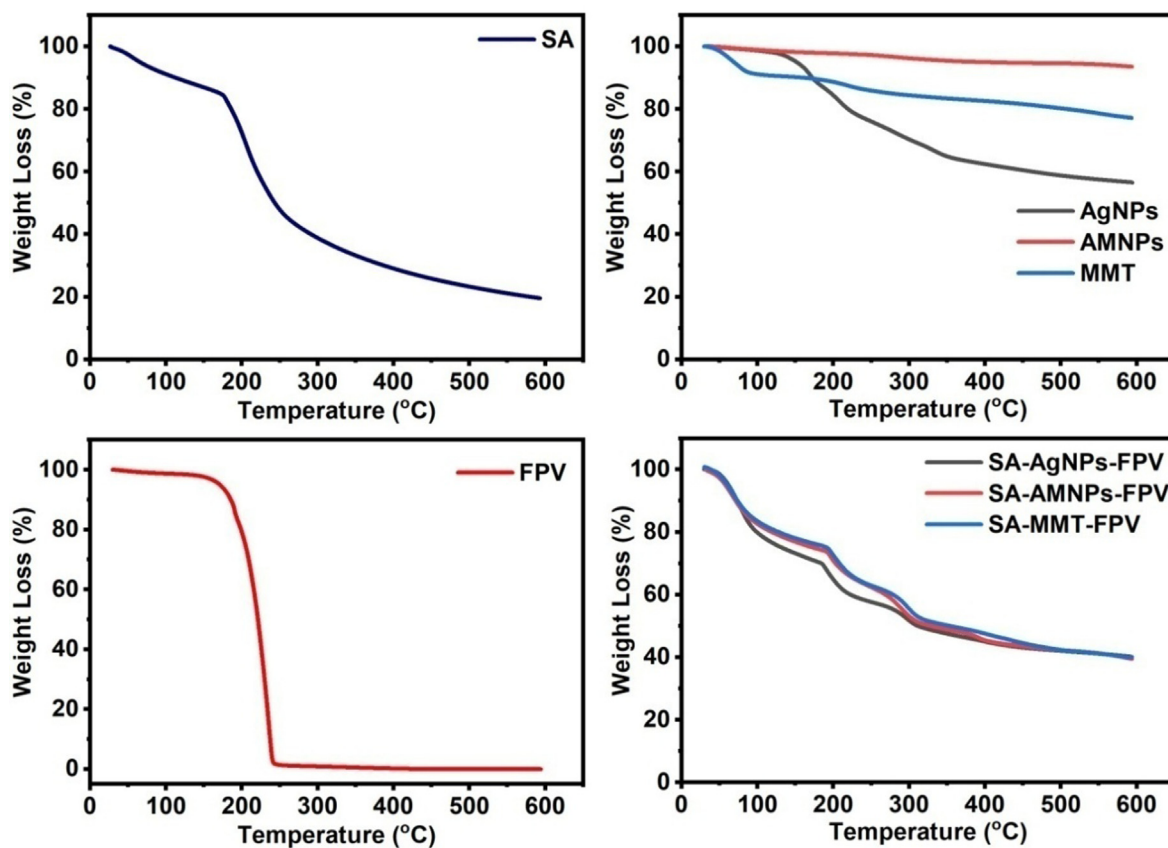


Fig. 4 TGA curves of SA, FPV, AgNPs, AMNPs, MMT, SA-AgNPs-FPV, SA-AMNPs-FPV, and SA-MMT-FPV.

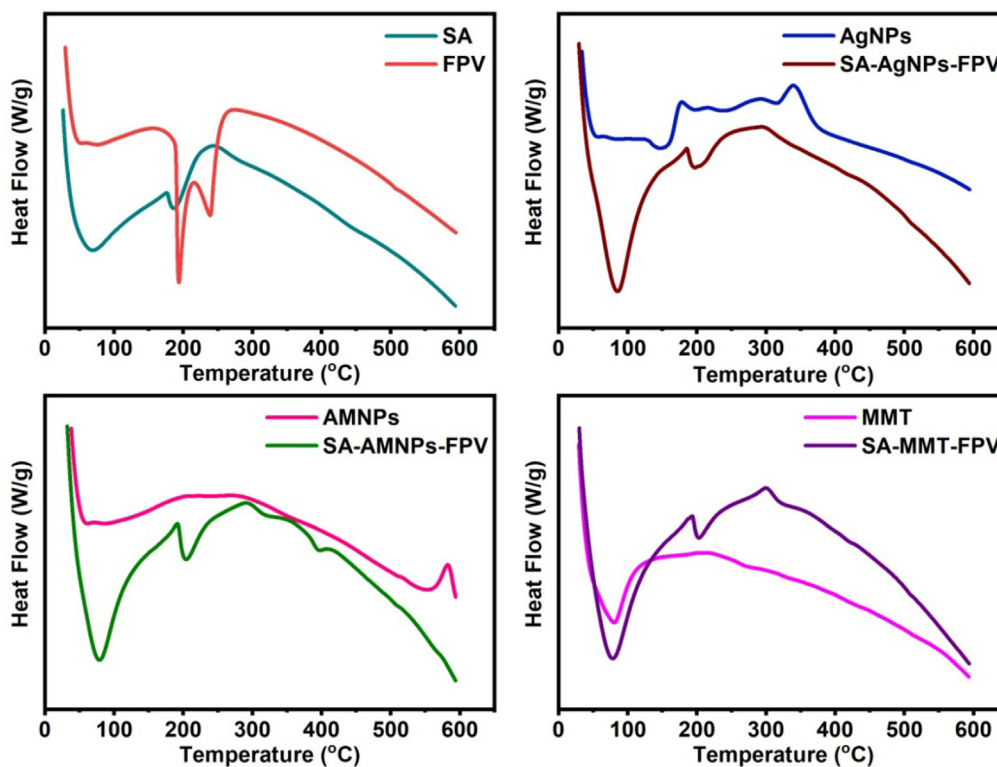


Fig. 5 DSC peaks of SA, FPV, AgNPs, SA-AgNPs-FPV, AMNPs, SA-AMNPs-FPV, MMT, and SA-MMT-FPV.

peaks were not seen in SA-AgNPs-FPV due to the stabilization of AgNPs by the SA matrix. The DSC pattern of MMT showed an endothermic peak at 80 °C, which is due to its melting point, and a slight exothermic peak at 207 °C. In the DSC pattern of SA-MMT-FPV, the MMT peaks were not observed, which indicates that MMT was stabilized by the SA matrix. The melting point peaks of FPV were not found in the drug-loaded microbeads (SA-AMNPs-FPV, SA-AgNPs-FPV, and SA-MMT-FPV), which indicated that the FPV had molecularly dispersed in the SA matrix.

3.4. XRD

To evaluate the crystalline nature of FPV, MMT, AgNPs, AMNPs and the dispersion of FPV at the molecular level in the SA matrix, XRD analysis was conducted, and the results were shown in Fig. 6. MMT exhibited prominent peaks at 8.47° and 25.95°, with a basal space of 0.103 nm at 8.47°, but this basal space was expanded to 0.124 nm following loading with FPV, indicating that the FPV molecules were successfully interacted with MMT of the SA-MMT-FPV matrix (Obireddy et al., 2021). XRD peaks of AgNPs at 38.1°, 46.2°, 67.4°, and 76.5° corresponded to the planes of (111), (200), (220), and (311), respectively (JCPDS card no. 04-0783). These results were in good agreement with the results of an XRD study of green synthesis of AgNPs by Mehta et al. (Mehta et al., 2017). The XRD peaks of AgNPs were observed in SA-AgNPs-FPV, indicating that AgNPs had been successfully incorporated into the SA matrix. Similarly, the XRD peaks of AMNPs at 30.3°, 35.7°, 43.4°, 54.2°, 57.3°

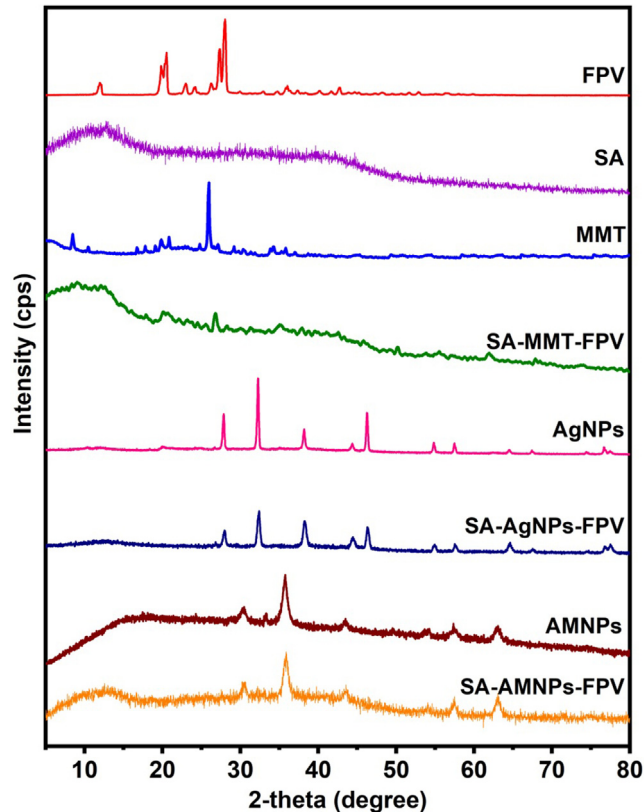


Fig. 6 XRD patterns of FPV, SA, MMT, SA-MMT-FPV, AgNPs, SA-AgNPs-FPV, AMNPs, and SA-AMNPs-FPV.

and 62.9° were assigned to the (220), (311), (400), (422), (511) and (440) planes, respectively (JCPDS card no. 19-0629) (Obireddy and Lai 2022). The XRD peaks of FPV were observed between 10 and 30° , indicating the crystalline nature of FPV. These peaks were not found in SA-MMT-FPV, SA-

AgNPs-FPV, and SA-AMNPs-FPV microbeads, suggesting that the FPV molecules had converted their crystalline nature to amorphous nature in the SA matrix. Hence, FPV molecules were dispersed at the molecular level in the SA matrix (Poudel and Kim 2021).

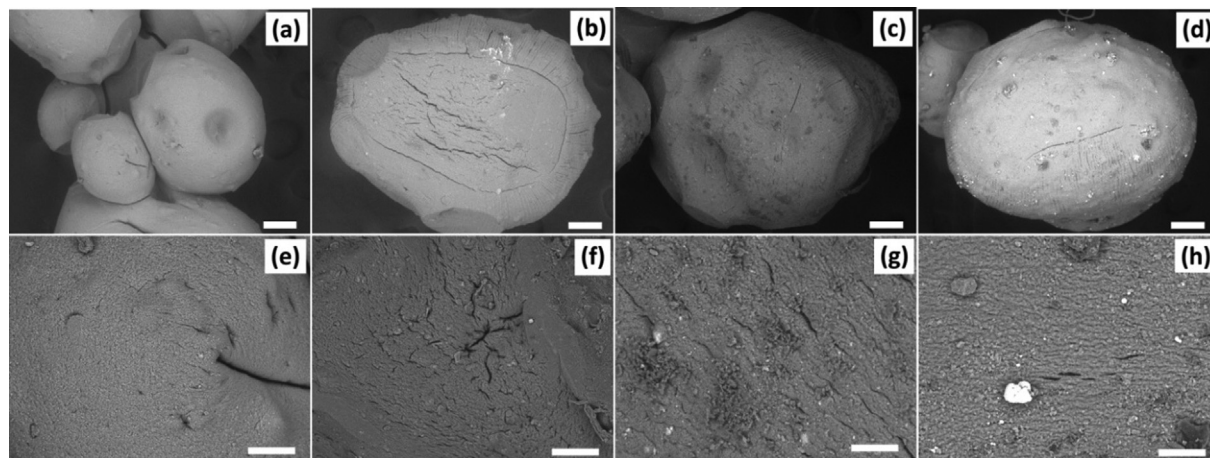


Fig. 7 The SEM images of SA (a & e), SA-AgNPs-FPV (b & f), SA-AMNPs-FPV (c & g), and SA-MMT-FPV (d & h). Scale bar = $100\ \mu\text{m}$.

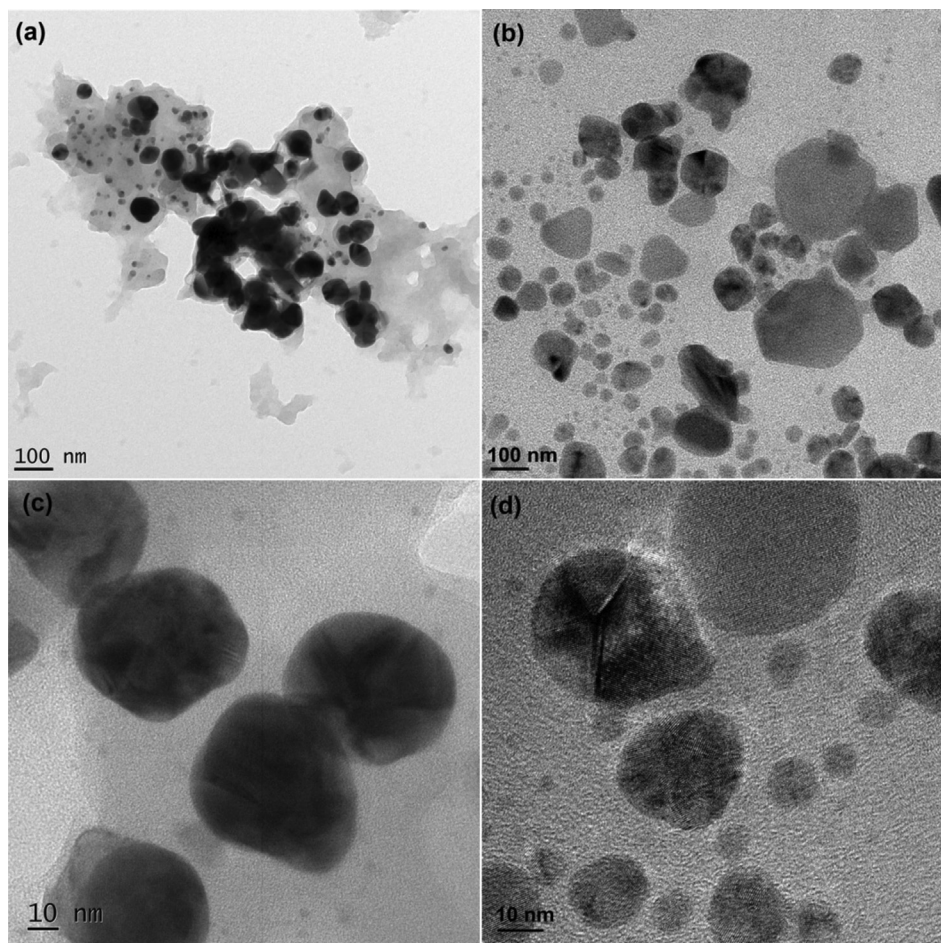


Fig. 8 TEM images of AMNPs (a&c) and AgNPs (b&d).

3.5. SEM and TEM

SEM examination was conducted to investigate the topology of the developed microbeads, and the images were shown in Fig. 7. The SEM analysis clearly showed that the surface of SA microbeads was smooth in nature, whereas the surface of the SA-AgNPs-FPV, SA-AMNPs-FPV, and SA-MMT-FPV microbeads was rough and porous in nature. In comparison to SA-AgNPs (and SA-AMNPs-FPV), the surface of SA-MMT-FPV microbeads has more roughness, indicating that MMT platelets were found on the surface of the microbeads. SA-AgNPs-FPV more porous than SA-AMNPs-FPV because AgNPs had fewer interactions with the SA matrix than AMNPs, since AMNPs had amine functional groups, which made them more likely to interact with the SA matrix. The sizes of the generated nanoparticles was analyzed by HR-TEM analysis and the results were shown in Fig. 8. It was concluded that the size of NPs was between 10 and 30 nm.

3.6. Encapsulation efficiency and in vitro drug release studies

The %EE of SA-AgNPs-FPV, SA-AMNPs-FPV, and SA-MMT-FPV microbeads were 41, 43, and 47%, respectively. The results showed that the percentage EE of SA-MMT-

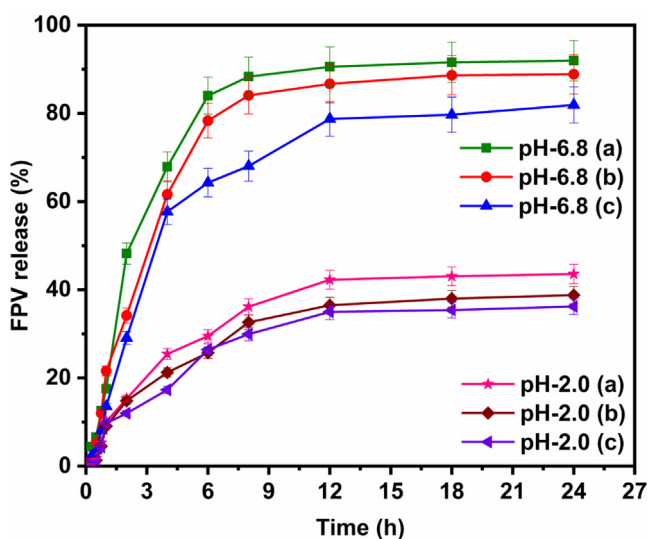


Fig. 9 *In vitro* release studies of SA-AgNPs-FPV(a), SA-AMNPs-FPV (b), and SA-MMT-FPV(c) in PBS of pH 6.8 and 2.0 at 37 °C.

FPV was higher than that of the SA-AgNPs-FPV and SA-AMNPs-FPV microbeads owing to the good absorption capacity and a large specific area of MMT that facilitated hydrogen bonding between FPV molecules of O–H and N–H groups with the hydroxyl groups of MMT. As a result, the percentage EE of FPV in SA-MMT-FPV was higher than that of the SA-AgNPs-FPV and SA-AMNPs-FPV microbeads. *In vitro* release studies were performed at pH 2.0 and pH 6.8. The results in Fig. 9 showed that the release rate was higher at pH 6.8 than at pH 2.0. This was because the carboxylate group showed less interaction with the buffer at pH 6.8, the network slackened and the permeability increased, allowing a more easy release of the drug. At lower pH, ionic-ionic repulsions occurred between proton (H^+) ions and the polymer matrix to hinder solvent penetration into the polymer matrix, resulting in lower release rates at pH 2.0 than at pH 6.8 (Mumper et al., 1994, Sanchez-Ballester et al., 2019). Comparison between the release behaviour of SA-AgNPs-FPV and other formulations showed that the release rate was higher because SA-AgNPs-FPV had a more porous nature, which resulted in the penetration of solvent molecules into the polymeric matrix. The network then became loose, and consequently the drug release rate was high, whereas in the case of SA-AMNPs-FPV and SA-MMT-FPV, the release rate was low because the AMNPs and MMT interacted strongly with the polymeric matrix. As a result, the surface became less porous, which meant that a tight network structure had been built, and the release rate was slower. In addition, MMT formed hydrogen with FPV molecules and intercalated FPV molecules with the alumina silicate layers of MMT, therefore the inter-layer FPV molecules could not be exchanged completely with PBS media (Obireddy et al., 2021). Hence, a lower release rate was observed in SA-MMT-FPV than in other formulations. In addition, the release rate was lowered because the FPV had low solubility at pH 2.0, whereas at pH 6.8, the solubility was high, hence the release rate was high at pH 6.8. These results were in good agreement with the results of the FPV solubility analysis of Goktug et al. (Göktuğ et al., 2021).

3.7. Release kinetics

To determine the release kinetics of our developed microbeads, the release data were fitted into various kinetic models (zero order, first order, Higuchi model, and Korsmeyer-Peppas model), and the resulting r^2 values were listed in Table 1. The release kinetics of the developed microbeads were consistent with the Higuchi model, indicating that the drug release method involved the penetration of PBS media into the algi-

Table 1 Release kinetics parameters of SA-AgNPs-FPV, SA-AMNPs-FPV, and SA-MMT-FPV in PBS of pH 2.0 and 6.8 at 37 °C.

Code	Temp.	pH	Zero		First order		Higuchi		Korsmeyer-Peppas	
			K_0	r^2	K_1	r^2	K_H	r^2	n	r^2
SA-AgNPs-FPV	37 °C	6.8	5.533	0.565	0.169	0.9752	22.648	0.901	0.840	0.983
		2.0	2.468	0.756	0.035	0.8859	9.888	0.942	0.847	0.994
SA-AMNPs-FPV	37 °C	6.8	5.268	0.633	0.143	0.9733	21.406	0.905	0.900	0.990
		2.0	2.178	0.763	0.029	0.8748	8.722	0.946	0.849	0.997
SA-MMT-FPV	37 °C	6.8	4.435	0.693	0.096	0.9567	17.887	0.911	0.944	0.988
		2.0	2.037	0.763	0.027	0.8646	8.147	0.935	0.881	0.983

nate matrix and diffusion of the drug molecules into external media. This finding fits well with Higuchi's model, which describes the development of many theoretical frameworks for understanding the release of low-soluble drugs from solid and semi-solid matrices (Bruschi 2015). In this study, we used FPV as a model drug, which had low solubility; hence, the developed microbeads followed the Higuchi model for release kinetics. Additionally, to ascertain the mechanism of the microbeads, the release data were fitted to the Korsmeyer-Peppas equation, with the corresponding n and r^2 values displayed in Table 1. The values of n ranged between 0.983 and 0.997, demonstrating that the microbeads followed a Super Case-II transport mechanism, which meant the drug release rate was governed by the relaxation of the polymeric chains.

4. Conclusions

Alginate is a naturally occurring polysaccharide that has been widely exploited in drug delivery because of its high biocompatibility, easy processing, and gelling capability under mild conditions. Over the years, alginate-based materials have been fabricated in various forms, ranging from nanoparticles to fibres, for encapsulation and sustained release of therapeutic agents. Yet, most of the alginate-based systems show poor drug release sustainability because of the high erosion rate of alginate-based hydrogels. The situation is worsened when poorly soluble drugs are loaded. Due to the poor affinity of the drug molecules to the gel matrix formed by alginate, the encapsulation efficiency and release sustainability were highly limited. This problem could be partially addressed by modifying the properties of the gel matrix using inorganic modifiers. In this study, we used favipiravir as a model of poorly soluble drugs to examine the effect of three inorganic nanoparticulate modifiers (montmorillonite clay material, silver nanoparticles, and iron-based magnetic nanoparticles) on the encapsulation and sustained release of drug. Our results showed that incorporation of different nanoparticulate modifiers into alginate-based nanoparticles led to changes in porosity and hydrophilicity (and hence drug encapsulation efficiency and release sustainability), even though little effect on the mechanism of drug release was observed. Results from this study provide insights into the modification of gel-based nanoparticles for encapsulation and sustained release of poorly soluble drugs.

Declaration of Competing Interest

The authors declare that they have no known competing financial interests or personal relationships that could have appeared to influence the work reported in this paper.

References

- Abasalizadeh, F., Moghaddam, S.V., Alizadeh, E., et al, 2020. Alginate-based hydrogels as drug delivery vehicles in cancer treatment and their applications in wound dressing and 3D bioprinting. *J. Biol. Eng.* 14, 8. <https://doi.org/10.1186/s13036-020-0227-7>.
- Akbarzadeh, A., Samiei, M., Davaran, S., 2012. Magnetic nanoparticles: preparation, physical properties, and applications in biomedicine. *Nanoscale Res. Lett.* 7, 144. <https://doi.org/10.1186/1556-276X-7-144>.
- Boddu, A., Obireddy, S.R., Zhang, D., et al, 2022. ROS-generating, pH-responsive and highly tunable reduced graphene oxide-embedded microbeads showing intrinsic anticancer properties and multi-drug co-delivery capacity for combination cancer therapy. *Drug Deliv.* 29, 2481–2490. <https://doi.org/10.1080/10717544.2022.2100512>.
- Bruschi, M.L., 2015. Mathematical models of drug release. Strategies to Modify the Drug Release from Pharmaceutical Systems. Woodhead Publishing, Cambridge, pp. 63–86.
- Carretero, M.I., Pozo, M., 2009. Clay and non-clay minerals in the pharmaceutical industry: part I. excipients and medical applications. *Appl. Clay Sci.* 46, 73–80. <https://doi.org/10.1016/j.clay.2009.07.017>.
- Chandrakala, V., Aruna, V., Angajala, G., 2022. Review on metal nanoparticles as nanocarriers: current challenges and perspectives in drug delivery systems. *Emerg. Mater.* 5, 1593–1615. <https://doi.org/10.1007/s42247-021-00335-x>.
- Chintha, M., Obireddy, S.R., Areti, P., et al, 2020. Sodium alginate/locust bean gum-g-methacrylic acid IPN hydrogels for “simvastatin” drug delivery. *J. Dispers. Sci. Technol.* 41, 2192–2202. <https://doi.org/10.1080/01932691.2019.1677247>.
- Costa, P., Sousa Lobo, J.M., 2001. Modeling and comparison of dissolution profiles. *Eur. J. Pharm. Sci.* 13, 123–133. [https://doi.org/10.1016/S0928-0987\(01\)00095-1](https://doi.org/10.1016/S0928-0987(01)00095-1).
- Elmowafy, E.M., Tiboni, M., Soliman, M.E., 2019. Biocompatibility, biodegradation and biomedical applications of poly(lactic acid)/poly(lactic-co-glycolic acid) micro and nanoparticles. *J. Pharm. Invest.* 49, 347–380. <https://doi.org/10.1007/s40005-019-00439-x>.
- Galdiero, S., Falanga, A., Vitiello, M., et al, 2011. Silver nanoparticles as potential antiviral agents. *Molecules* 16, 8894–8918. <https://doi.org/10.3390/molecules16108894>.
- Göktuğ, Ö., Altaş, E., Kayar, G., et al, 2021. The development and the validation of a novel dissolution method of favipiravir film-coated tablets. *Sci. Pharm.* 90, 3.
- Huang, Y., Tao, Q., Hou, D., et al, 2017. A novel ion-exchange carrier based upon liposome-encapsulated montmorillonite for ophthalmic delivery of betaxolol hydrochloride. *Int. J. Nanomed.* 12, 1731–1745. <https://doi.org/10.2147/IJN.S122747>.
- Hun Kim, M., Choi, G., Elzatahry, A., et al, 2016. Review of clay-drug hybrid materials for biomedical applications: administration routes. *Clays Clay Miner.* 64, 115–130.
- Jat, S.K., Gandhi, H.A., Bhattacharya, J., et al, 2021. Magnetic nanoparticles: an emerging nano-based tool to fight against viral infections. *Mater. Adv.* 2, 4479–4496. <https://doi.org/10.1039/D1MA00240F>.
- Jeremiah, S.S., Miyakawa, K., Morita, T., et al, 2020. Potent antiviral effect of silver nanoparticles on SARS-CoV-2. *Biochem. Biophys. Res. Commun.* 533, 195–200. <https://doi.org/10.1016/j.bbrc.2020.09.018>.
- Jiao, W., Chen, W., Mei, Y., et al, 2019. Effects of molecular weight and guluronic acid/mannuronic acid ratio on the rheological behavior and stabilizing property of sodium alginate. *Molecules* 24. <https://doi.org/10.3390/molecules24234374>.
- Jyoti, K., Baunthiyal, M., Singh, A., 2016. Characterization of silver nanoparticles synthesized using *Urtica dioica* Linn. leaves and their synergistic effects with antibiotics. *J. Radiat. Res. Appl. Sci.* 9, 217–227. <https://doi.org/10.1016/j.jrras.2015.10.002>.
- Kota, S., Dumpala, P., Anantha, R.K., et al, 2017. Evaluation of therapeutic potential of the silver/silver chloride nanoparticles synthesized with the aqueous leaf extract of *Rumex acetosa*. *Sci. Rep.* 7, 11566. <https://doi.org/10.1038/s41598-017-11853-2>.
- Krupskaya, V.V., Zakusin, S.V., Tyupina, E.A., et al, 2017. Experimental study of montmorillonite structure and transformation of its properties under treatment with inorganic acid solutions. *Minerals* 7. <https://doi.org/10.3390/min7040049>.
- Kumar, R., Nayak, M., Sahoo, G.C., et al, 2019. Iron oxide nanoparticles based antiviral activity of H1N1 influenza A virus. *J. Infect. Chemother.* 25, 325–329. <https://doi.org/10.1016/j.jiac.2018.12.006>.
- Lee, K.Y., Mooney, D.J., 2012. Alginate: properties and biomedical applications. *Progr. Polym. Sci.* 37, 106–126. <https://doi.org/10.1016/j.progpolymsci.2011.06.003>.

- Li, P., Dai, Y.-N., Zhang, J.-P., et al, 2008. Chitosan-alginate nanoparticles as a novel drug delivery system for nifedipine. *Int. J. Biomed. Sci.* 4, 221–228.
- Li, T., Zhao, L., Zheng, Z., et al, 2018. Design and preparation acid-activated montmorillonite sustained-release drug delivery system for dexibuprofen in vitro and in vivo evaluations. *Appl. Clay Sci.* 163, 178–185. <https://doi.org/10.1016/j.clay.2018.07.026>.
- Mehta, B.K., Chhajlani, M., Shrivastava, B.D., 2017. Green synthesis of silver nanoparticles and their characterization by XRD. *J. Phys.: Confer. Ser.* 836. <https://doi.org/10.1088/1742-6596/836/1/012050>
- Mumper, R.J., Huffman, A.S., Puolakkainen, P.A., et al, 1994. Calcium-alginate beads for the oral delivery of transforming growth factor- β 1 (TGF- β 1): stabilization of TGF- β 1 by the addition of polyacrylic acid within acid-treated beads. *J. Control. Release.* 30, 241–251. [https://doi.org/10.1016/0168-3659\(94\)90030-2](https://doi.org/10.1016/0168-3659(94)90030-2).
- Niraimathi, K.L., Sudha, V., Lavanya, R., et al, 2013. Biosynthesis of silver nanoparticles using *Alternanthera sessilis* (Linn.) extract and their antimicrobial, antioxidant activities. *Colloids Surf. B* 102, 288–291. <https://doi.org/10.1016/j.colsurfb.2012.08.041>.
- Obireddy, S.R., Lai, W.-F., 2022. ROS-generating amine-functionalized magnetic nanoparticles coupled with carboxymethyl chitosan for pH-responsive release of doxorubicin. *Int. J. Nanomed.* 17, 589–601. <https://doi.org/10.2147/IJN.S338897>.
- Obireddy, S.R., Subbarao, S.M.C., Venkata, K.R.K.S., et al, 2021. Development and characterization of montmorillonite-based hybrid materials for pH-responsive drug delivery. *ChemistrySelect* 6, 1466–1470. <https://doi.org/10.1002/slct.202004711>.
- Pirtarighat, S., Ghannadnia, M., Baghshahi, S., 2019. Green synthesis of silver nanoparticles using the plant extract of *Salvia spinosa* grown in vitro and their antibacterial activity assessment. *J. Nanostruct. Chem.* 9, 1–9. <https://doi.org/10.1007/s40097-018-0291-4>.
- Poudel, S., Kim, D.W., 2021. Developing pH-modulated spray dried amorphous solid dispersion of candesartan cilexetil with enhanced in vitro and in vivo performance. *Pharmaceutics* 13, 497. <https://doi.org/10.3390/pharmaceutics13040497>.
- Rautela, A., Rani, J., Debnath, M., 2019. Green synthesis of silver nanoparticles from *Tectona grandis* seeds extract: characterization and mechanism of antimicrobial action on different microorganisms. *J. Anal. Sci. Technol.* 10, 5. <https://doi.org/10.1186/s40543-018-0163-z>.
- Reddy, O.S., Subha, M.C.S., Jithendra, T., et al, 2019. Emerging novel drug delivery system for control release of curcumin through sodium alginate/poly (ethylene glycol) semi IPN microbeads-intercalated with kaolin nanoclay. *J. Drug Delivery Ther.* 9, 324–333.
- Rizwana, H., Alwhibi, M.S., Al-Judaie, R.A., et al, 2022. Sunlight-mediated green synthesis of silver nanoparticles using the berries of *Ribes rubrum* (red currants): characterisation and evaluation of their antifungal and antibacterial activities. *Molecules* 27, 2186.
- Samuel, M. S., M. Ravikumar, A. John J, et al., 2022. A review on green synthesis of nanoparticles and their diverse biomedical and environmental applications. *Catalysts*. 12, 459
- Sanchez-Ballester, N.M., Soulairol, I., Bataille, B., et al, 2019. Flexible heteroionic calcium-magnesium alginate beads for controlled drug release. *Carbohydr. Polym.* 207, 224–229. <https://doi.org/10.1016/j.carbpol.2018.11.096>.
- Sung, Y.K., Kim, S.W., 2020. Recent advances in polymeric drug delivery systems. *Biomater. Res.* 24, 12. <https://doi.org/10.1186/s40824-020-00190-7>.
- Teja, A.S., Koh, P.-Y., 2009. Synthesis, properties, and applications of magnetic iron oxide nanoparticles. *Prog. Cryst. Growth Charact. Mater.* 55, 22–45. <https://doi.org/10.1016/j.pcrysgrow.2008.08.003>.
- Thimmaiah, P.G., Mudinepalli, V.R., Thota, S.R., et al, 2022. Preparation, characterization and dielectric properties of alginate-based composite films containing lithium silver oxide nanoparticles. *Front. Chem.* 9, 777079.
- Zheng, X., Dou, J., Yuan, J., et al, 2017. Removal of Cs^+ from water and soil by ammonium-pillared montmorillonite/ Fe_3O_4 composite. *J. Environ. Sci.* 56, 12–24. <https://doi.org/10.1016/j.jes.2016.08.019>.